Dynamic Digital Image Correlation Method For Rolling Convective Contact

Nehemiah Mork[a], Antonia Antoniou[a] and Michael J. Leamy[a,*]

[a]The Woodruff School of Mechanical Engineering, Georgia Institute of Technology, Atlanta, 30318, Georgia, USA

ARTICLE INFO

Keywords:
Digital image correlation
Ncorr
Large rotation
BRISK feature detection
Rolling contact

ABSTRACT

Digital image correlation (DIC) is an increasingly popular and effective non-contact method for measuring full-field displacements and strains of deformable bodies under load. Current DIC methods applied to bodies undergoing large displacements and rotations require a large measurement area for both the reference (i.e., undeformed) image and the deformed images. This can limit the resulting resolution of the displacement and strain fields. To address this issue, we propose a two-stage dynamic DIC method capable of measuring displacements and strains under material convection with high resolution. During the first stage, the reference image is assembled from smaller, high-resolution images of the undeformed object obtained using a spatially-fixed or moving frame. Following capture, each sub-image is rigidly translated and rotated into its appropriate place, thereby producing a full, high-resolution image of the reference body. In stage two, images of the loaded and deformed body, again obtained using a small camera frame with high resolution, are aligned with matching regions of the undeformed composite image using BRISK feature detection before performing DIC. We demonstrate the method on a contact problem whereby an elastomeric roller travels along a rigid surface. In doing so, we obtain fine-resolution measurements of the state of strain of the region of the roller sidewall in contact with the substrate, even as new material convects through the region of interest. We present these measurements as a series of images and videos capturing strain evolution as the roller transitions from static loads to a fully dynamic steady-state, documenting the effectiveness of the method.

1. Introduction

Digital image correlation (DIC) has proven to be an effective scale-agnostic, non-contact method for measuring full field deformation under static or dynamic loading. Both 2D and 3D-DIC has been applicable to a wide range of applications including the study of crack propagation [1–9], tensile testing [10–14], pressure vessel analysis [15–20], and in the study of a wide range of contact mechanics problems. These contact mechanics problems include impact analysis [21] such as Taylor impact testing of Aluminum 5083 [22], low velocity impact on composite plates [23], water backed impact [24], and vibro-impact [25]. DIC has also been extensively utilized for slip experiments to measure relative slip in fretting fatigue of a variety of materials [26–29]. Similarly, it has been employed to determine material contact stiffness through displacement measurements up to gross slip [30].

Recent work has utilized DIC to monitor deformation along roller sidewalls and contact areas to provide insight into rolling and slipping contact mechanics. The stick-slip behaviour of tire blocks sliding on a glass plate has been analyzed using DIC to determine slip propagation and cyclic stick-slip behavior [31]. A similar study was performed using DIC to measure deformation of tire tread blocks during cornering and slip initiation [32]. Still others measured the displacement and strain fields of an elastomeric roller under quasistatic normal and tangential loading along the roller

*Corresponding author: michael.leamy@me.gatech.edu
ORCID(s):

sidewall and contact area [33]. For fully dynamic studies, a camera mounted on the undercarriage of a vehicle has been used to track feature points on a tire and the ground [34]. By tracking displacement of feature points between frames, the tire speed and ground speed were calculated, allowing estimation of the tire longitudinal slip-ratio. Similarly, a tire's longitudinal slip ratio has been measured as it traverses rough terrain as well as measuring wheel lockup during sudden breaking [35]. The vibrational charactersitics of a rolling tire were measured using both laser Doppler vibrometry and DIC [36]. While DIC provides an efficient and accurate alternative to laser vibrometry, the image resolution limits the high frequency spectra. Gao *et al.* performed a series of studies implementing DIC to measure the sidewall displacement and strain of a rolling tire at different speeds. A single point of interest was tracked on the tire sidewall as it rotated through the contact region. In the first work, the principle strain was calculated and used to measure the contact length of the tire [37]. In the second work, the principle strain was used to calculate the rolling resistance, and the authors documented strong agreement with other experimental methods [38]. Finally, in the third work the influence of multiple different tire pressures and vertical loads on the resulting tire deformation was observed [39].

One challenge in applying DIC to rolling problems is that the procedure must account for large rotations of the deformed image relative to the reference image. In the aforementioned work by Gao *et al.*, an improved method based on the absolute nodal coordinate formulation (ANCF) was employed [37–39]. Rather than dividing the image into subset regions where DIC is performed locally, the ANCF method decomposes the image into small elements where the global nodal position coordinates and nodal position-vector gradient coordinates are used as searched parameters [40, 41]. Since the global coordinates and position-vector gradients are defined as the nodal coordinates under the absolute nodal coordinate system, there is no limitation on the amount of deformation and rotation of each element [38]. An alternative approach is to implement an initial value estimation procedure to rapidly account for large rotation before taking into account fine tuning. Wang *et al.* presented such a procedure using a multiresolution analysis method based on a wavelet pyramid for initial value estimation [42]. Large rotation is accounted for quickly at lower resolutions before matching the reference and deformed images at higher resolutions. Still another method introduced a polar coordinate DIC method where the subsets are circular and rotations of these subsets are easily accounted for in polar coordinates [43].

Performing DIC on dynamic problems is a challenge due to requiring all pixels within the region of interest to be present in both the undeformed and deformed versions of the image. When an object begins to rotate, old pixels leave the field of view and new pixels enter the field of view thus making DIC difficult. A common method for circumventing this issue is to image the entire object during dynamic loading. While the previously reviewed works effectively account for large rotations, they still require imaging the entire rolling object within each frame, or they use a second method which measures the relative displacement and strain between two successive frames. Imaging the entire object within each frame can limit the possible resolution in regions of interest (such as contact zones). Additionally, measuring

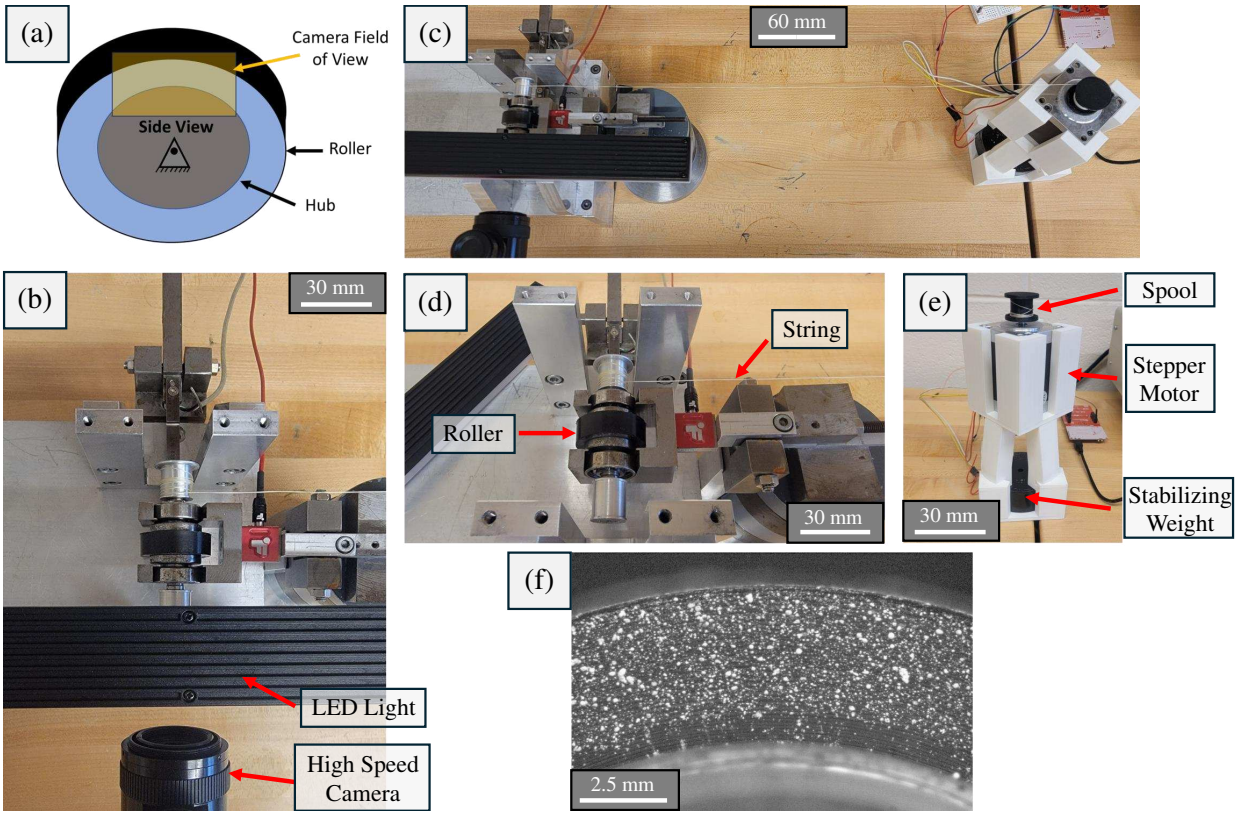

Figure 1: Experimental setup for capturing undeformed images of the roller. (a) Conceptual schematic for imaging the undeformed roller with the field of view highlighted. (b) top view of the roller housing. The roller sidewall is imaged using a high speed camera. (c) The roller is rotated using stepper motor which winds the string on a spool. Since the string is wrapped around the axle of the roller the rolling rotates at a consistent speed. (d) Close up view of the roller and axle with the string wrapped around the axle. (e) Stepper motor stand and support. (f) Example image obtained during testing.

relative deformation, while beneficial, does not capture the total strain (i.e., referencing an undeformed configuration). In contrast, this work proposes a dynamic DIC method providing high-resolution strain fields in a pre-selected region of interest, even as material continually convects through it. In such scenarios, the reference image of the pre-selected image bears little resemblance to the deformed tire after just a small amount of rotation. While the implementation of this procedure is general and can be applied to a multitude of loading scenarios and geometries, we demonstrate it using contact between a rolling elastomer and a rigid substrate. Only the region of the roller sidewall in the contact zone is imaged and analyzed, enabling high-resolution strain measurements using a small frame of view, while minimizing the computational burden and storage requirements.

The presented procedure is broken into two stages. The first stage requires imaging the undeformed roller and assembling the undeformed images to create a single high resolution composite image of the undeformed roller. This stage is done once and the resulting imaging can be re-used for any number of loading cases/scenarios. Loading and deformation then commence and a second stage aligns deformed images of the roller sidewall with sections of the

undeformed composite image using BRISK feature detection [44], a computer vision algorithm that has been developed to address invariance in rotation, scale transformation and noise in groups of features. The BRISK detection is done prior to DIC analysis. For sufficiently large applied loads, the alignment between deformed and undeformed sections is fine tuned using the open source DIC software Ncorr [45]. As documented herein, the two-stage DIC procedure produces smooth videos of the strain fields within the contact zone as the roller transitions from static loading to a fully dynamic steady-state, capturing transient phenomena in between. The MATLAB code as well as high speed images and videos discussed in this work are accessible from the authors' SourceForge website [46]

2. Overview of Two-Stage Dynamic DIC Procedure and Setup

The proposed DIC procedure is decomposed into two stages. Using a spatially-fixed camera frame and a center-fixed, rotating roller, small sections of the undeformed roller's sidewall are first imaged consecutively using a Chronos 14-1.1-34M camera with a maximum speed of 1069 frames per second and pixel resolution of 1024 by 1280 - see Fig. 1 (a). These images are then used to assemble a composite reference image of the undeformed roller. Lens distortion was addressed using checkerboard calibration through MATLAB [47], specifically implemented on a WMT-050-0.5-C checkerboard containing 61×61 squares each of dimension 50mm $\times$ 50 mm. The field of view only includes the part of the roller sidewall close to the point of contact since that is the region of interest. The experimental apparatus employed for securing and imaging the roller is documented in detail in Ref. [33]. As displayed in Fig. 1 (b), the elastomeric roller is placed on a rigid steel hub. The axle of the roller is free to rotate due to roller bearings on each side of the roller connecting the roller axle to the housing. The housing is maintained at a set height during the undeformed imaging. The free rotation of the roller is controlled using a stepper motor as depicted in Fig. 1 (c) by wrapping a string around the axle of the roller as displayed in Fig. 1 (d). The stepper motor shown in Fig. 1 (e) is stabilized during activation using a mass at the base of the stand. The stepper motor used in this work is a NEMA 23 bipolar stepper motor using a step angle of 1.8° (200 steps/revolution) and drawing 1 A at 8.6 V with a holding torque of 14 kg-cm. The stepper motor is driven at half steps for smooth rotation resulting in a step size of 0.9° and 400 steps/revolution. The stepper motor is driven by a DRV8825 stepper motor driver controlled by an MSP432 Texas Instruments microcontroller. During undeformed rotation, the stepper motor drives the roller at a rate of 16 rpm. An example image captured during undeformed rolling is presented in Fig. 1 (f).

In the second stage, loading is applied and the deformed roller is imaged, as described below. The deformed images are compared to a matching undeformed section of the composite roller image to assist with calculating the current strain field. As depicted in Fig. 2 (a), the imaging field of view remains the same as in the first stage; however, the roller now experiences both a normal and tangential load. The normal load forces the roller against the substrate while the tangential load is applied at the hub of roller and points leftward, imposing a counterclockwise torque. Figure 2

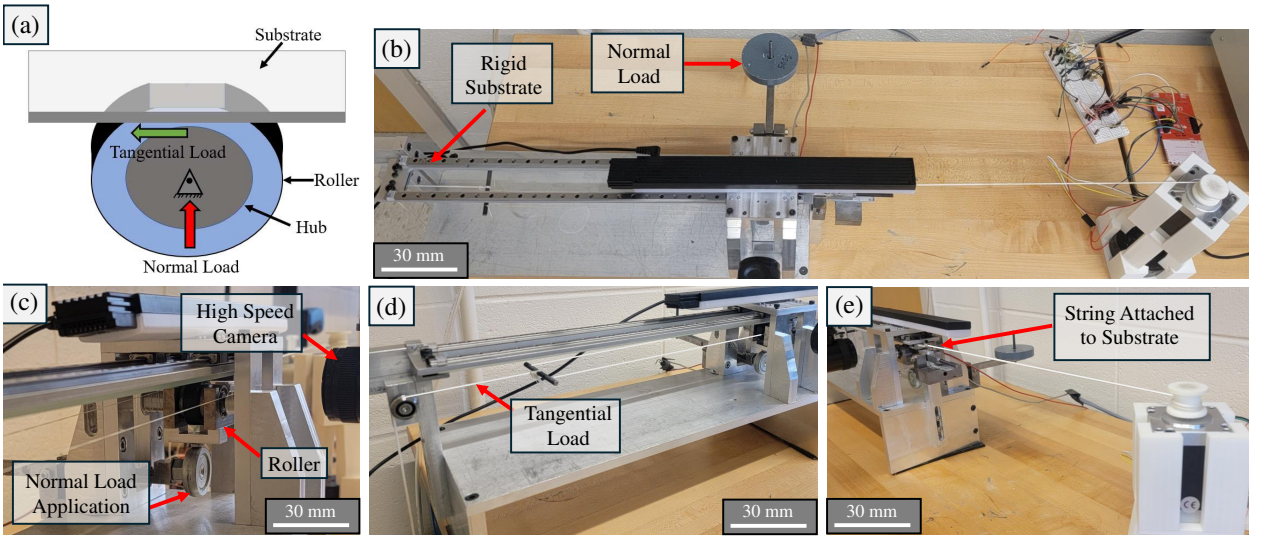

Figure 2: Experimental setup for imaging the deformed roller. (a) Conceptual diagram for imaging the deformed roller. The camera field of view is consistent with the undeformed imaging. The roller experiences both normal and tangential loads. (b) Top view of the testing setup. A normal load is applied to press the roller against the rigid substrate. The substrate is translated horizontally by the motor and initializes rotation of the roller. The roller's sidewall is imaged using a high speed camera. (c) The normal load presses the roller housing upwards and the tangential loads are applied tangentially to the roller hub. (d) The tangential load is applied to the roller by wrapping two strings around the axle of the roller which are tensioned using a steel mass (not visible). (e) A string connects the rigid substrate to the stepper motor. The stepper motor winds the string which translates the substrate and initializes rotation of the roller.

(b) provides a top view of the entire experimental setup. The clear glass substrate translates uniaxially along linear rails. One end of the substrate is attached to the stepper motor spool, and the other end is attached to a large driving weight (not shown; see [33]), such that as the stepper motor winds the string, the substrate translates from left to right. Figures 2 (b) and (c) show how the normal load is applied to the roller. A steel disk presses downwards on a lever which converts this force into an upward force pressing the roller against the substrate. Figures 2 (c) and (d) show the manner in which a second load tangential to the roller hub is applied to the roller. A string wrapped around each end of the roller hub is tied to a rigid, threaded, steel rod. A single string then runs from this threaded rod to a pulley and down to a second steel disk weight. The steel weight applies tension to the strings imposing a tangential load. During loaded rolling, the roller is driven at a speed of 3.5 seconds per revolution.

Herein we analyze two loading scenarios. The first scenario uses 0.5 kg masses to apply the normal ($N_{0.5}$) and tangential ($T_{0.5}$) loads. The resulting normal and tangential loads are equal to 4.9 N. The second loading scenario uses 2 kg masses to apply normal (N_2) and tangential (T_2) loads. The resulting loads are equal to 19.6 N.

The elastic roller is the same as that used in Refs. [33] and [48] and has an outer diameter of 30 mm, an inner diameter of 20 mm, and a thickness of 10 mm in the axial direction. It is fabricated from Sylgard 184 PDMS and black paint. After fabrication, the roller has an expected elastic modulus of 1.85 MPa and Poisson's ratio of 0.495. The sidewall and roller circumference are coated with a random speckle pattern. The speckles have an average diameter of

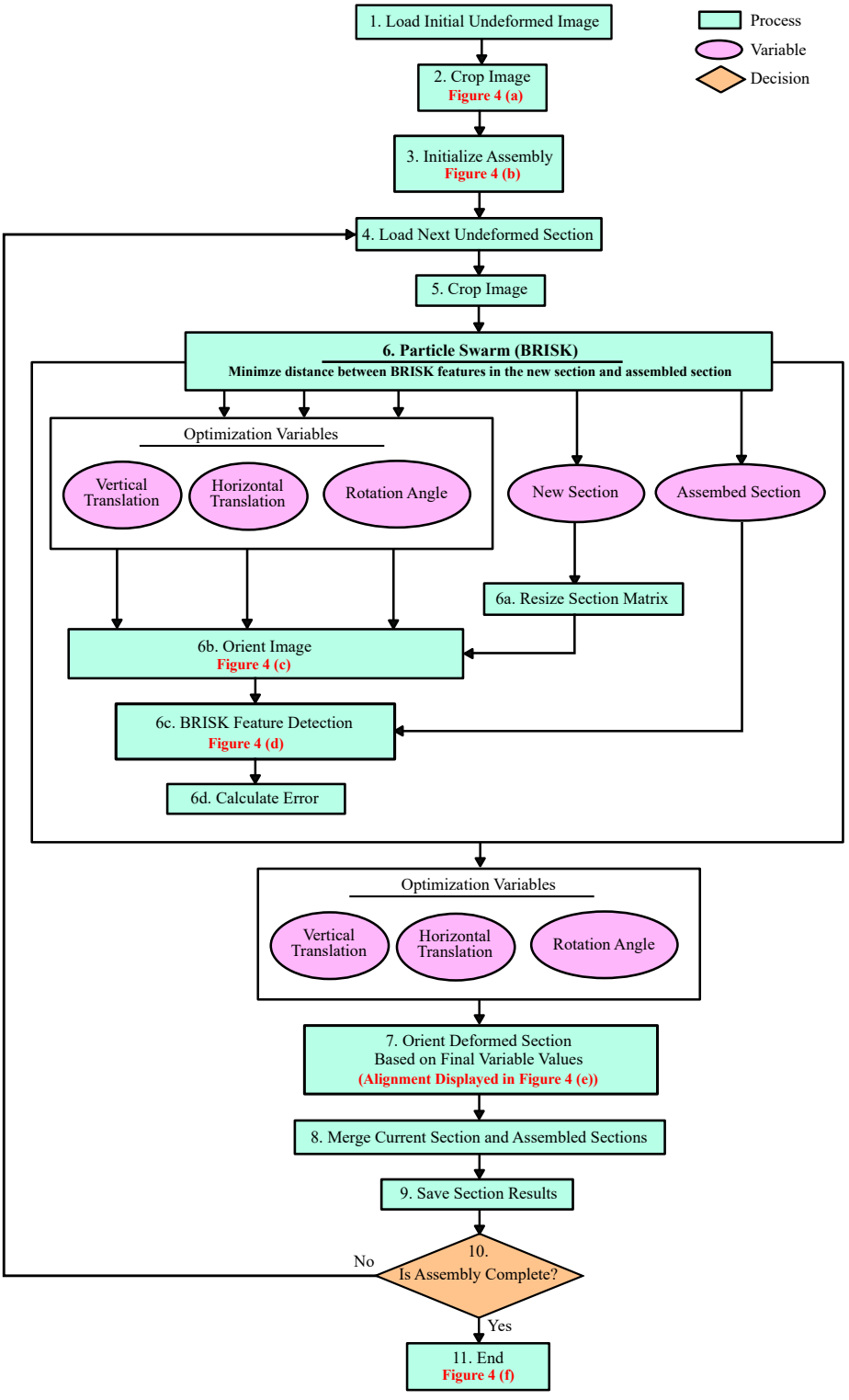

Figure 3: Process flow chart for assembling the composite reference (i.e., undeformed) image. The code implements one round of global optimization using the particle swarm algorithm which minimizes the desired error. In this case the error is the distance between feature points in the new undeformed section and current assembled composite section. Once the optimum location and orientation of the new undeformed section is determined, it is merged with the assembled composite section and the assembled composite section is updated. This process is repeated until the entire undeformed roller is assembled.

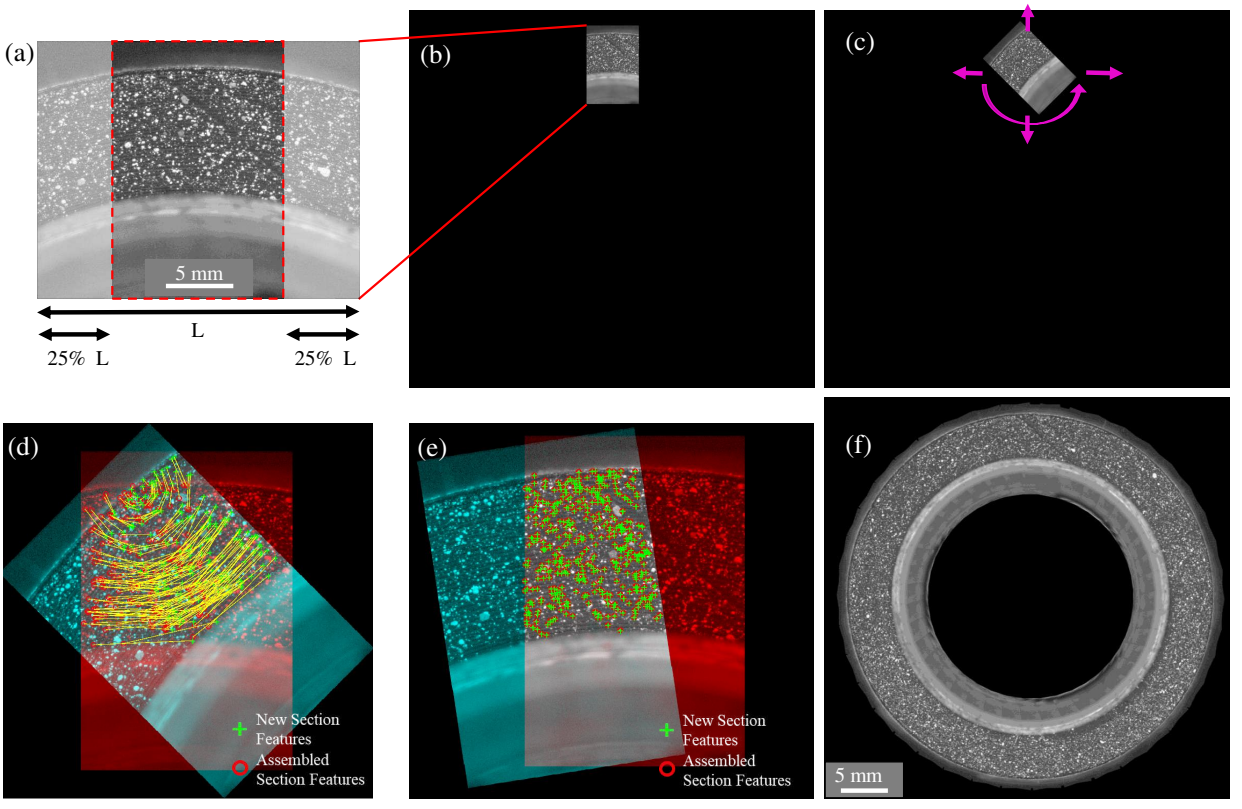

Figure 4: Procedure for assembling the full undeformed composite reference image. (a) Each frame of the undeformed roller is first cropped to minimize distortion. (b) The first undeformed image is placed into an empty matrix that is capable of containing the full undeformed roller image initiating the composite image. (c) Subsequent undeformed images are cropped and placed into their own empty full matrices. (d) The BRISK feature detection algorithm is performed on both the composite image matrix and the new section matrix. The features in each image are matched with green crosses marking the new section features and red circles representing the assembled section features with yellow lines connecting feature pairs. (e) A particle swarm algorithm is run to minimize the displacement between the feature points between the new section and assembled sections. (f) The full undeformed reference image results from the assembly of all sections.

0.07 mm using mostly white, but also gold and green paints. Lastly, the roller is heat treated at 75 °C for an hour to cure the speckles to the roller surface. The PDMS preparation and curing protocol along with material properties can be found in detail in Ref. [33].

3. Reference Image Assembly

Once the undeformed images are collected, they are combined one at a time to assemble the composite reference image. Figure 3 provides the assembly process flowchart. Each step in Fig. 3 is linked to the discussion here by use of parentheses, e.g. (1) refers to step 1 in Fig. 3. First we load the initial undeformed image (1) before cropping it (2), as depicted in Fig. 4 (a). These images are loaded into MATLAB as matrices of grayscale 8 bit unassigned integers with the dimensions equivalent to the pixel dimensions of the loaded image (1024×1280 resulting from the chosen camera's resolution). Cropping the image is optional and its only purpose is to minimize the distortion present in the

preserved portion of the roller. Even small distortion can cause error when aligning images. In this work we crop the image by removing 25% of the pixel columns on each edge. Once cropped, the image matrix is loaded into a separate empty uint8 matrix of sufficient size to hold the entire composite image, as shown in Fig. 4 (b) (3). The size of the matrix can be determined based on the size of the initial frame or dynamically resized as necessary. In this work we used a pre-sized matrix (6144×7168) and refer to it as the "full matrix" due to it being able to hold the full undeformed roller image. This full matrix is never rotated or transformed and thus the size of this matrix only affects computation time through feature detection, which we introduce later. The cropped section image is "loaded" into the full matrix by setting a group of pixels in the full matrix equal to the cropped image's uint8 values, essentially transferring the cropped image into the full matrix. The placement of the first imaged section within the full matrix can be chosen based on known information of the geometry, or if unknown, can be placed arbitrarily, although a larger full matrix may be required. As we see in Fig. 4 (b) the section is placed in the top middle of the image which allows the roller to be built around the first image. Once the composite image is initialized using the first frame, the following frames are fit one at a time to the assembled composite image. Similar to the first frame, the frames are loaded (4) and cropped (5) before entering a particle swarm algorithm which globally searches for the best alignment of the current frame to the composite section.

A brief outline of the alignment process is described next (6). The particle swarm algorithm is a global optimization algorithm we use to vary the location and orientation of the new section within its full matrix in order to minimize an error measure. This error is based on tracking the distance between common features in both the current and composite images. By minimizing the distance between common feature points, the current frame is near-seamlessly aligned with the current composite image. BRISK feature detection is used with the particle swarm algorithm to locate common feature pairs between these images, allowing for the calculation of the distance between the same features in both images, which is used as the particle swarm error measure. We implement the BRISK feature detection algorithm due to its balance of accuracy and computational efficiency. We have found the BRISK feature detection to be significantly faster per point than other available approaches, such as SIFT, SURF, or KAZE feature detection algorithms. BRISK also detects more feature points than alternatives, but has a higher density of points at corners instead of across the surface of the image. ORB detection is another valid detection method that is comparable to BRISK in its accuracy and speed. However, ORB tends to generate a very large number of points and so the required memory is large and the matching time between sets of feature points can be excessive. Overall, BRISK was found to be the most efficient balance between speed and corner accuracy. For a more in depth comparison between these feature detection methods, the reader is referred to Refs. [49] and [44]. Note that the code provided in the linked SourceForge [46] has been written such that any feature detection algorithm can be utilized. The user simply calls a different built-in feature detection method or calls a separately written feature detection function.

To align the images based on feature detection, a global search algorithm is required since the error is not guaranteed to be smooth. We select particle swarm as the global search algorithm since it is efficiently implemented through the global optimization toolbox in MATLAB and can run many iterations in parallel, reducing the required computational time. In addition, it is simple to implement and does not require calculation of the gradient of the solution curve. For an in-depth description and analysis of the particle swarm algorithm, the reader is referred to Refs. [50–52]. The first step in the particle swarm alignment process orients the current frame within the full matrix. As depicted in Fig. 4 (c), the optimization parameters for the location of the current frame within the empty full matrix are the horizontal and vertical placement as well as the counter-clockwise rotation of the current frame. The current frame is padded with zeros based on its rotation angle prior to rotation so that it rotates without further cropping of the image (6a). It is then rotated with cubic interpolation and placed into its own empty full matrix (6b). We now have two matrices of equal size, one which contains the currently-assembled sections (Fig. 4 (b)) and one that only contains the new section (Fig. 4 (c)). BRISK feature detection is then performed on each matrix to extract the feature points of the images (6c). The features of each image are matched to track common feature point pairs between the new undeformed image and the assembled composite image. Figure 4 (d) shows an overlay of the two images with common features marked as green crosses for the new section image, and red circles for the assembled image. The particle swarm algorithm minimizes the average distance (i.e., error) between feature points of these two images; yellow lines in the figure visualize the distance between common features (error between a single feature pair). The error equation for the average distance between feature points is

$$\frac{\sum_{j=1}^{N} \sqrt{(x_1^{(j)} - x_2^{(j)})^2 + (y_1^{(j)} - y_2^{(j)})^2}}{N}, \tag{1}$$

where N denotes the number of feature point pairs, $(x_1^{(j)}, y_1^{(j)})$ denotes the feature point location in pixels of the first image, and $(x_2^{(j)}, y_2^{(j)})$ denotes the feature point location in pixels of the second image (6d). The particle swarm algorithm varies the horizontal and vertical locations, and rotation angle, of the new undeformed section within the full matrix until it converges to a global error minimum. Note that it is not uncommon for a few errors to exist when matching feature points between the two images resulting in feature pairs that are comprised of differing features. We implement a filter that calculates the distance between feature point pairs and removes feature point pairs that result in distant outliers. For the filter we utilize the built-in *isoutlier()* MATLAB function to detect local outliers using a moving window of a specified length. This is implemented in the code using the command *isoutlier(f, "movmedian", 30)* where 'f' is an array of distances between feature pairs and the moving window is 30 values long. This was found to be a sufficient filtering method.

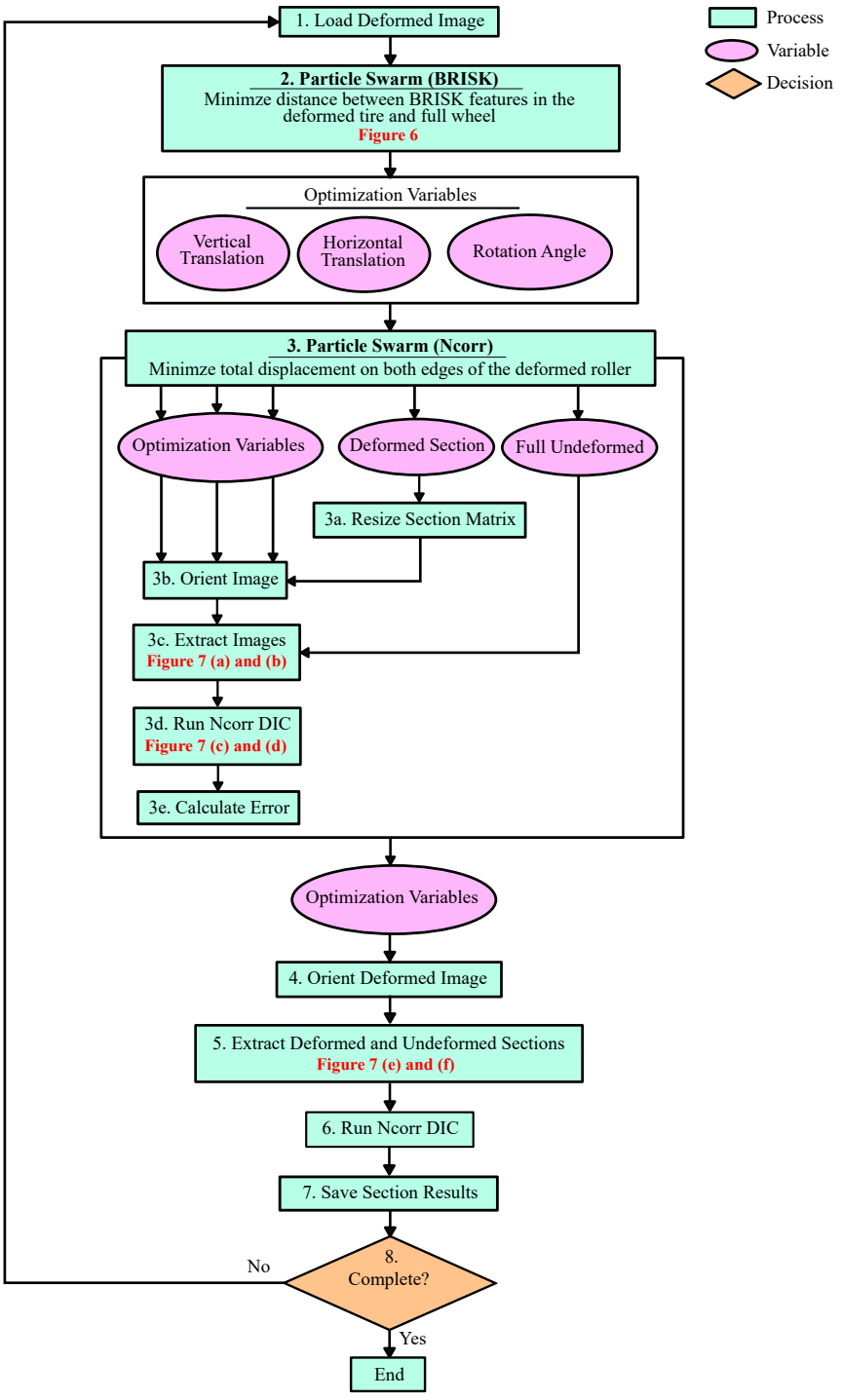

Figure 5: Process flow chart for matching deformed images with their matching undeformed section of the full reference composite image and calculating the resulting deformation. The code implements two rounds of global optimization using the particle swarm algorithm which minimizes the desired error. In the first round the error is the distance between feature points in the deformed section and undeformed composite image. The second round fine tunes the optimization variables and uses the displacement calculated by the DIC software Ncorr as the particle swarm error. Once the optimum location and orientation of the deformed image is determined, Ncorr calculates the deformation between the deformed image and the section of the undeformed composite image.

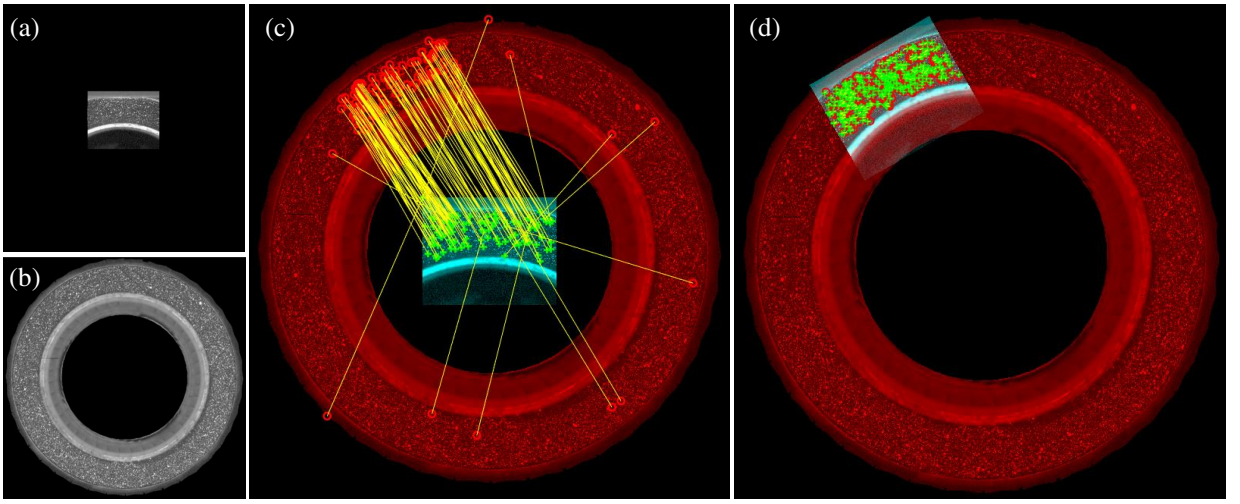

Figure 6: Process to match deformed images to their respective locations along the full roller composite image. (a) Deformed section loaded into an empty full matrix. (b) Full composite reference image. (c) BRISK is performed between the full matrix containing the deformed section and the full matrix containing the composite reference image. The particle swarm algorithm minimizes the distance between the common feature points. (d) The final solution for the example deformed image.

When the particle swarm algorithm converges to a final solution, it returns the optimized set of variables along with the minimum error and other statistics. The optimized variables are used to locate and orient the new section within the full matrix one last time (7). As Fig. 4 (e) documents, it is apparent the distance between feature points is minimal resulting in the new section aligning on top of the current assembled section. At this point the two matrices are merged and the assembled section is updated to include the new section (8). This is achieved by finding all elements that are not equal to zero in the full matrix containing the new section and carrying over those values to the same elements in the full matrix containing the assembled section. This is now the new assembled section. The variables are all saved (9) and the status of the program is checked to determine if this is the last frame to analyze (10). If it is not, a new section is loaded and the process continues, otherwise the procedure ends. Figure 4 (f) displays the full reference image produced using the described approach (11). This image needs only to be generated once and can then be reused for any number of loading cases/scenarios.

4. Deformed Image Alignment and Strain Calculation

Once the full undeformed composite image is assembled, we align the deformed images with their matching undeformed sections and calculate the strain within the current frame using the open source DIC software Ncorr [45]. Figure 5 outlines this process. Similar to Sec. 3, each step in Fig. 5 is linked to the discussion here by use of parentheses; e.g., (1) refers to step 1 in Fig. 5. Each deformed image is first loaded into the workspace (1) and then enters a particle swarm algorithm based on minimizing distance between BRISK features (2). The outline of

the particle swarm algorithm is the same as that in Fig. 3 for the undeformed image alignment and is used to align the deformed image on top of the matching undeformed section of the composite image. Figures 6 (a) and (b) present visualizations of the full matrices containing the deformed section and undeformed composite image, respectively. The BRISK algorithm is performed on both matrices to detect feature points. Figure 6 (c) presents the matching feature point pairs between the deformed section (green crosses) and the full undeformed roller (red circles) with yellow lines connecting the matching feature pairs. It is apparent from the figure that several errors are found when matching features between the deformed section and the full roller. The deformed section should align with the upper-left portion of the undeformed roller where the vast majority of the matching feature points are located. However, several errors are discovered where features in the deformed section are matched with features at various locations along the undeformed roller. These errors do not hinder the convergence of the deformed section's orientation and eventually are filtered out using the previously mentioned filter. Similar to the reference image assembly, the deformed section is aligned with the undeformed roller such that the average distance between feature points is minimized. As the location and orientation of the deformed section are updated to achieve this goal, the filter removes the errors which appear as outliers in the distance between matching feature point pairs. Figure 6 (d) presents the final solution the particle swarm algorithm converges upon with no errors remaining.

This first pass at orienting the deformed and undeformed images using BRISK features is efficient, but was found to lack the precision required, particularly for large loads, to accurately compute strains (and thus produce smooth strain images and videos) as material convects past the camera. In particular, the orientation of the deformed section is found to be dependent on the number of feature points as well as their distribution across the surface of the image, and thus there can be slight variations in final orientation between analyzed sections. Thus we implement a second global optimization to fine-tune the alignment between the images in which we integrate Ncorr to track the displacement of selected points that are equally spaced across the surface of the image (3). We use the final values of the optimized variables from the particle swarm algorithm based on BRISK feature detection as initial conditions for the second round of optimization. We also restrict the range of these variables to be centered around the final values obtained using particle swarm since the optimization integrated with Ncorr consumes significant computational time. Specifically, in the problem studied, the vertical and horizontal displacements of the frame are constrained to $\pm$ 40 pixels of the BRISK optimized displacements while the rotation is constrained to $\pm$ 4 degrees of the BRISK optimized angle. Consistent with the first round of optimization, the deformed image is zero-padded (3a) and then oriented in an empty full matrix (3b). The cells of the full matrix comprising the deformed image section are extracted and saved as the deformed image (3c). The same cells are then extracted from the full matrix that houses the undeformed composite image of the roller and are saved as the matching undeformed section. At this point, we have two images: one that is a deformed section and one that is the matching undeformed version of the section.

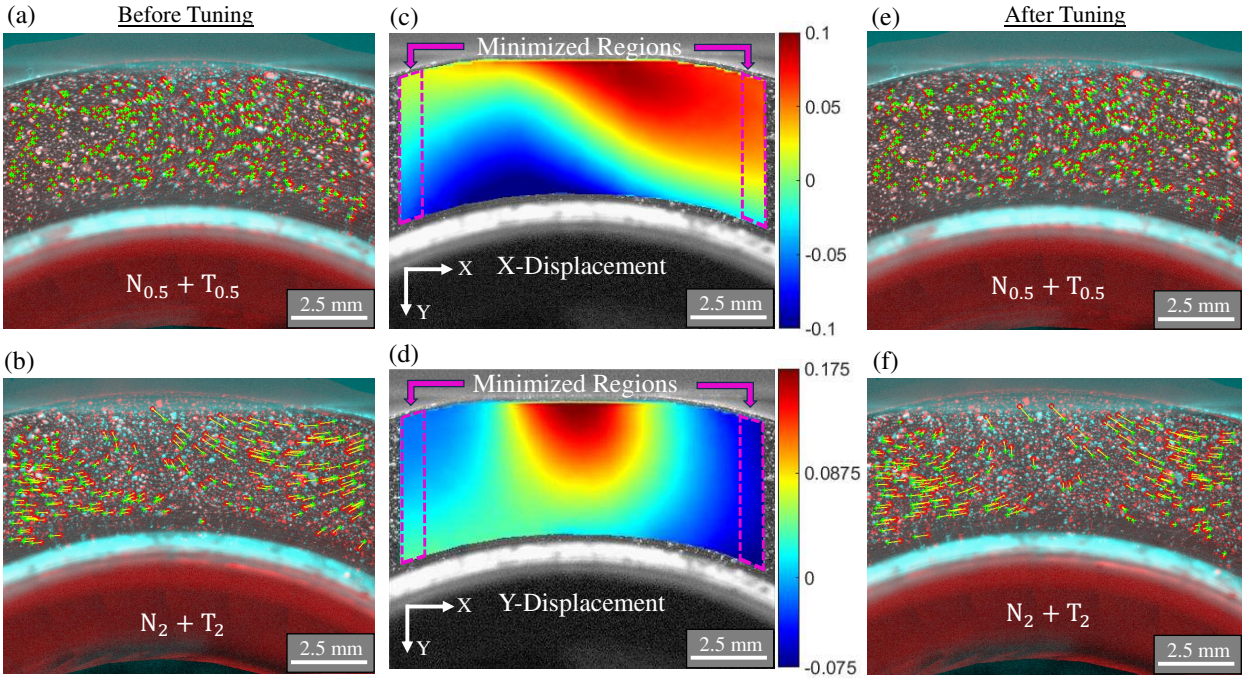

Figure 7: Using DIC to finely adjust the orientation of the undeformed section to center it along the deformed section. (a) Undeformed and deformed sections when the roller is under $N_{0.5}$ and $T_{0.5}$ loads after swarm optimization minimizes the distance between BRISK features. (b) Undeformed and deformed sections when the roller is under N_2 and T_2 loads after swarm optimization minimizes the distance between BRISK features. (c) X-displacement field with minimized regions outlined in magenta dashed lines on both edges. (d) Y-displacement field with minimized regions outlined in magenta dashed lines on both edges. (e) Undeformed and deformed sections when the roller is under $N_{0.5}$ and $T_{0.5}$ after swarm optimization minimizes the distance using Ncorr. (f) Undeformed and deformed sections when the roller is under N_2 and T_2 loads after swarm optimization minimizes the distance using Ncorr.

Figure 7 (a) displays the overlaid images of the extracted deformed image and matching section of the undeformed composite image for the roller for the case of $N_{0.5}$ and $T_{0.5}$ loads. It is apparent in the figure that BRISK detects many feature points across the entire surface of the deformed and undeformed images and does an accurate job of aligning the deformed section with its matching undeformed image. However, as observed in Fig. 7 (b) for N_2 and T_2 loading, the Brisk features detected are localized on the edges of the image. The feature localization is likely due to the large deformation of the elastic layer along the center of the image making it difficult to detect common features between the deformed and undeformed images. We note that features identified by BRISK are located along the edges of the image since there the roller experiences minimal deformation and thus the features are most similar to the undeformed image. In the case were the features are more heavily concentrated along one edge instead of evenly distributed across the surface, the optimization approach will result in an off-center alignment. When closely analyzed, Fig. 7 (b) reveals that the right edges of the images are misaligned.

To further optimize the alignment, we use Ncorr to calculate the displacement fields between the deformed section and its matching undeformed section (3d). Using Ncorr allows for tracking the displacement of more feature points than

provided by BRISK; in addition, these points are more evenly spaced across the surface of the image. Running Ncorr within the global optimization algorithm is time consuming, even while parallel processing, and so we implement sparse detection with a large subset spacing of 8 pixels (0.077 mm) where each subset is 30 pixels (0.29 mm). We then resize the displacement fields produced by Ncorr to match the resolution of the images using the *imresize()* function in MATLAB. This resizing is not as accurate as a lower subset spacing in Ncorr but is much faster and its accuracy is sufficient for the purpose of centering the images. Once the displacement fields are resized, the error of the current orientation of the deformed section is calculated to be the sum of displacements the first 100 columns of pixels experience on the right and left edges of the image, as we display in Fig. 7 (c) and (d) for the x and y displacements, respectively. For fine tuning with Ncorr, we use a modified error estimate,

$$\frac{\sqrt{(\sum_{j=1}^{N}(x_1^{(j)} - x_2^{(j)}))^2 + (\sum_{j=1}^{N} \mid (y_1^{(j)} - y_2^{(j)}) \mid)^2}}{N} \tag{2}$$

where N denotes the number of feature point pairs, $(x_1^{(j)}, y_1^{(j)})$ denotes the feature point location in pixels of the first image, and $(x_2^{(j)}, y_2^{(j)})$ denotes the feature point location in pixels of the second image (3e). This variation more heavily penalizes y-axis error. By orienting the deformed image such that the displacement is minimized along the edges of the image, we center the deformed section with its matching undeformed section. Figures 7 (e) and (f) present the overlaid deformed section and matching undeformed sections after fine-tuning using Ncorr for $N_{0.5} + T_{0.5}$ and $N_2 + T_2$ loading scenarios, respectively. It is apparent that Fig. 7 (e) does not experience as much deviation compared to Fig. 7 (a), which suggests that BRISK may be sufficient to center low deformation scenarios without utilizing the Ncorr fine tuning. Close inspection of Fig. 7 (f) shows greater deviation from its original alignment in Fig. 7 (b), and corrects the alignment at the right edge.

Once the second round of global optimization is completed, we orient the deformed image using the finalized parameter values (4), extract final image sections (5), run Ncorr for the last time (6), and save the resulting strain fields from the deformed and composite undeformed image (7). We use a subset spacing of 2 pixels (0.02 mm) for the $N_2 + T_2$ loading scenario and 3 pixels (0.029 mm) for the $N_{0.5} + T_{0.5}$ loading scenario. The lighter load tends to produce larger noise variation between subsets and so we use a larger spacing to filter this noise. Each subset is 30 pixels (0.29 mm) and has a strain radius of 15 pixels (0.15 mm). This process is repeated for each deformed frame (8).

5. Validation

We first verify that the composite undeformed roller image does not produce strain field artifacts due to meshing of multiple individual images. We obtain a deformed image of the roller sidewall after applying $N_{0.5}$ and $T_{0.5}$ loads to a roller pressed against a stationary substrate. We compute strain fields for this deformed image using as a reference

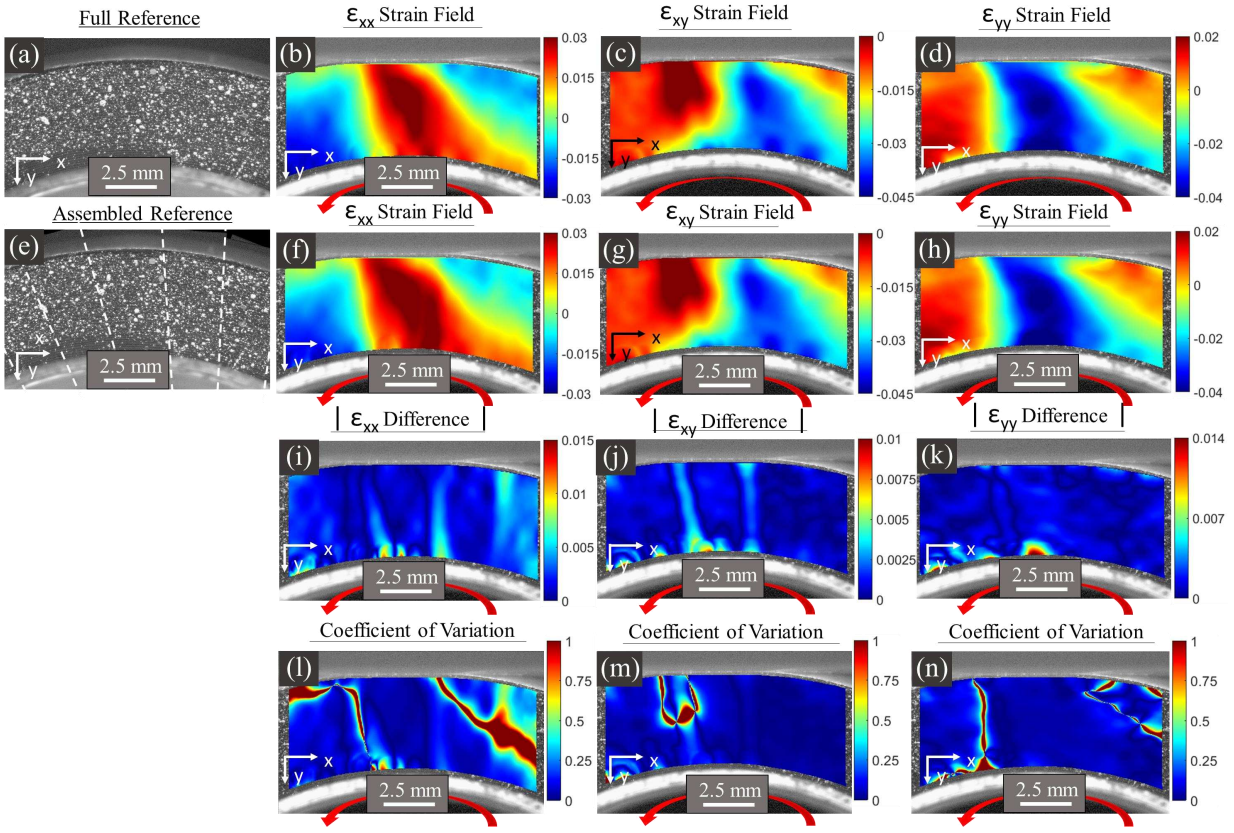

Figure 8: Comparison of strain fields produced along the roller sidewall using a single reference image or a composite reference image for $N_{0.5}$ and $T_{0.5}$ loads. (a) Single undeformed image of the roller sidewall that aligns with the deformed roller prior to rolling. (b)-(d) ε_{xx}, ε_{xy}, and ε_{yy} strain fields, respectively, using the single reference image in (a). (e) Composite reference image assembled by meshing six separate undeformed images. Dashed white lines mark the interface between individual images. (f) - (h) ε_{xx}, ε_{xy}, and ε_{yy} strain fields, respectively, using using the composite reference image in (e). (i) - (k) Differences in the ε_{xx}, ε_{xy}, and ε_{yy} strain fields, respectively. (l) - (n) Coefficient of variation between ε_{xx}, ε_{xy}, and ε_{yy} strain fields, respectively.

body either: (i) a single undeformed image of the roller section prior to loading, or (ii) a composite reference image obtained after performing the previously described two stage procedure. Figure 8 (a) presents the single undeformed reference image. Figures 8 (b) - (d) present the resulting $\varepsilon_{xx}, \varepsilon_{xy}$, and ε_{yy} strain fields calculated using Ncorr with this single unassembled reference image and the matching deformed image. In comparison, Fig. 8 (e) displays the reference image assembled using seven separate frames where dashed white lines demarcate the separate images composing the composite image. Figures 8 (f) - (h) present the resulting $\varepsilon_{xx}, \varepsilon_{xy}$, and ε_{yy} strain fields produced using Ncorr with this composite reference image and the deformed image.

To visualize the differences between strain fields (b) - (d) and (f) - (h), we subtract the two $\varepsilon_{xx}, \varepsilon_{xy}$, and ε_{yy} strain fields; Figs. 8 (i) - (k) display the results. As expected, error exists along the lines where separate images were merged to create the composite reference image. To assess the severity of this error, we also compute a coefficient of variation of each pixel. We first extract the strain values of the select pixel for each image. The two-sample ($n = 2$) standard

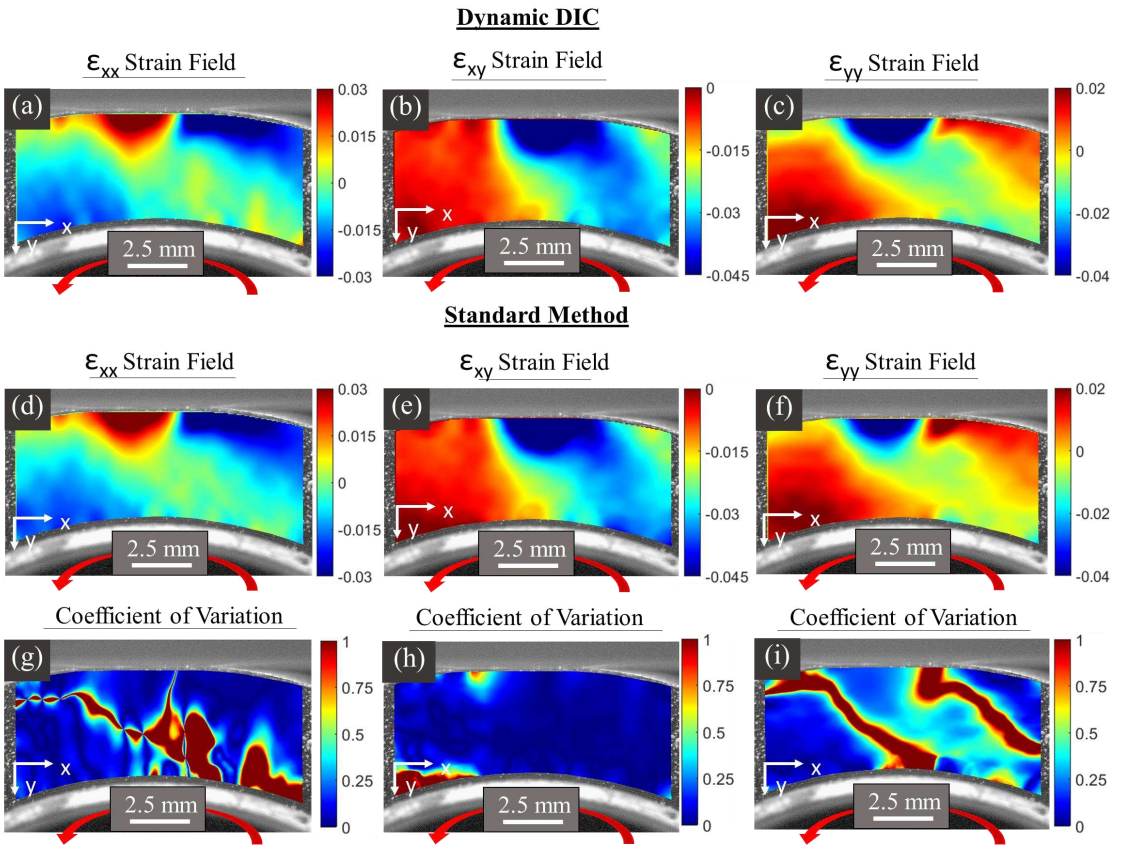

Figure 9: Comparison of strain fields produced after 90° rotation using both the dynamic DIC method as well as visual alignment between full high speed camera frames for $N_{0.5}$ and $T_{0.5}$ loads. (a) - (c) $\varepsilon_{xx}, \varepsilon_{xy}$, and ε_{yy} strain fields, respectively, calculated using the dynamic DIC method presented in this work. (d) - (f) $\varepsilon_{xx}, \varepsilon_{xy}$, and ε_{yy} strain fields, respectively, calculated using Ncorr on the deformed roller section after 90° rotation and the matching undeformed section captured during undeformed roller imaging. (g) - (i) Coefficient of variation between $\varepsilon_{xx}, \varepsilon_{xy}$, and ε_{yy} strain fields, respectively.

deviation is first calculated as well as the mean of the two values. The coefficient of variation is then calculated by dividing the standard deviation by the mean. Large coefficients of variation signify that the variation in pixel values between the two images is significant in comparison to the pixel value, while small coefficients signify a change in value that is insignificant in comparison to the pixel value. We desire these coefficient values to be as close to zero as possible but anything below one is significant since that signifies that the pixel variation is smaller than its magnitude. Figures 8 (l) - (n) present the calculated coefficients of variation between the strain fields produced using the single reference and assembled reference image for $\varepsilon_{xx}, \varepsilon_{xy}$, and ε_{yy} strain fields, respectively. It can be observed that the coefficient of variation is greatest around the border of the high strain regions since small deviations in the size of the high strain regions results in a large change in strain. We note that the coefficient of variation is significantly smaller than one along the meshing lines, providing confidence that the meshing error is relatively small.

We next verify that after significant rotation, the dynamic DIC algorithm preserves its accuracy. Figures 9 (a) - (c) present the $\varepsilon_{xx}, \varepsilon_{xy}$, and ε_{yy} strain fields, respectively, produced by the dynamic DIC algorithm after 90° rotation. This

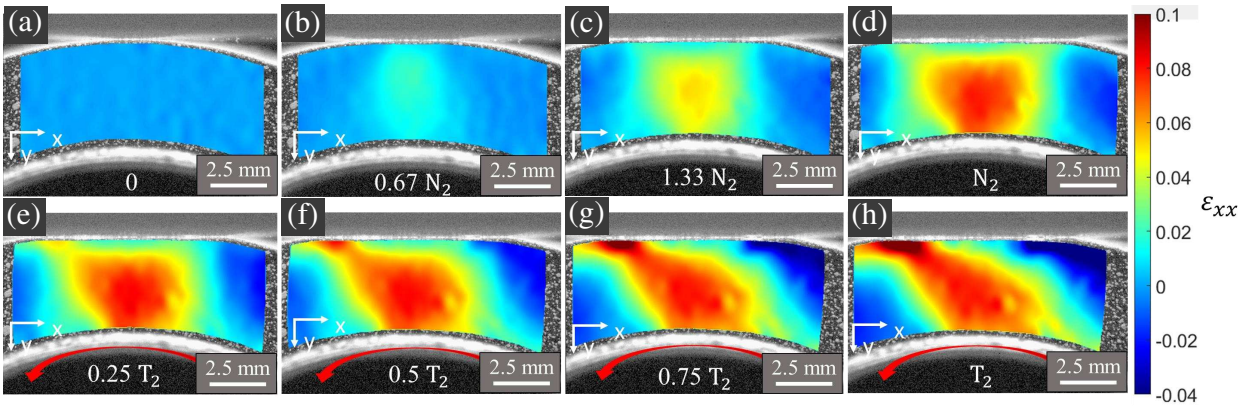

Figure 10: Example ε_{xx} strain fields during loading of the roller. The roller is first loaded normally to N_2 and then tangentially loaded to T_2. (a) - (d) Normal loading increases up to N_2 with no tangential load. (e) - (h) Normal load remains N_2 as the tangential load increases up to T_2.

angle was selected since, as we will see in the next section, this is the rotation at which steady state is achieved. Figures 9 (d) - (f) present the $\varepsilon_{xx}, \varepsilon_{xy}$, and ε_{yy} strain fields, respectively, produced using Ncorr on the deformed roller image after 90° rotation and the image of the undeformed roller section that matches, which was captured during undeformed roller imaging. The undeformed roller is rotated slowly during imaging so that we are able to select an undeformed section frame that closely aligns with the deformed section frame after 90° rotation. To verify that the dynamic DIC method remains consistent with the classic method of performing Ncorr on reference and deformed versions of the same roller section, we quantify the variation between the strain fields using the coefficient of variation presented in Fig. 8 (l) - (n). We present these coefficients of variation in Fig. 9 (g) - (i). It is apparent from the images that the coefficients of variation remain small (< 1) for the great majority of the fields. Regions of high variations exist, mainly around the border of high strain regions where the coefficient of variation is most sensitive similar to Fig. 8 (l) - (n). Overall the fields show strong agreement confirming the consistency and accuracy of the dynamic DIC method even after significant rotation.

6. Results and Discussion

With confidence in our strain fields established, we measure the strain fields resulting from quasistatic loading of the elastomeric roller with the substrate remaining stationary. We apply normal loading up to N_2 over 0.8 seconds followed by tangential loading up to T_2 over 1.8 seconds. The tangential load is applied slower than the normal load to avoid initiating rotation of the roller due to slipping. We calculate the $\varepsilon_{xx}, \varepsilon_{xy}$, and ε_{yy} strain fields at every fifth frame captured by the high speed camera and assemble them into short videos (see Vids. S1 - S3 in Supplementary Information). All videos henceforth are assembled using the same procedure and use the same color bars and video orientation as the figures presented in the text. Figure 10 presents the ε_{xx} strain field evolution produced by first

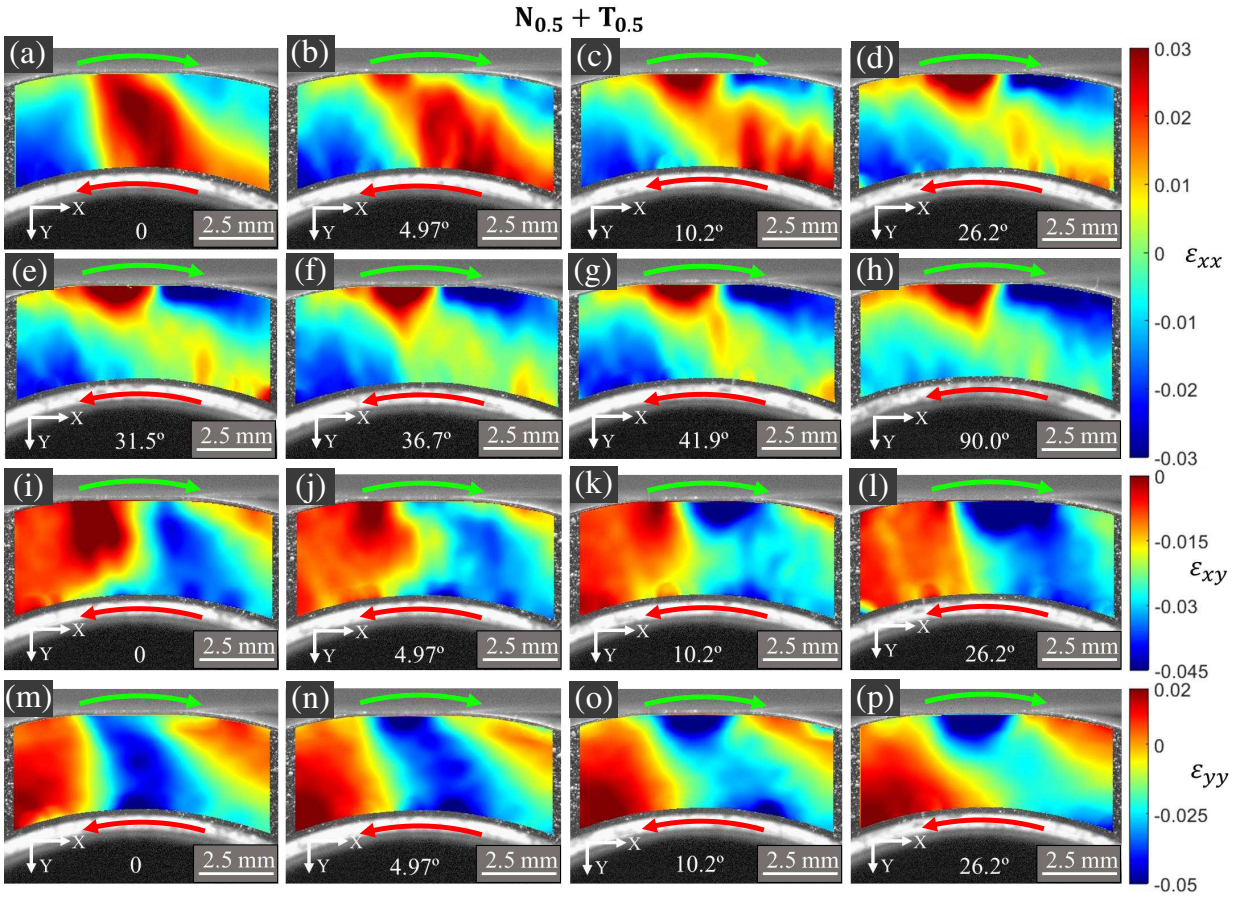

Figure 11: Strain fields produced during the onset of rolling when the roller transitions from quasistatic to dynamic steady-state for the $N_{0.5} + T_{0.5}$ loading scenario. The rotation direction of the roller is marked as a green arrow above the roller in each image and the imposed torque due to the tangential load is marked as a red arrow on the roller hub. (a) - (h) ε_{xx} strain fields moving from quasistatic in (a) to dynamic steady-state in (d) - (h). (i) - (l) ε_{xy} strain fields moving from quasistatic in (i) to dynamic steady-state in (l). (m) - (p) ε_{yy} strain fields moving from quasistatic in (m) to dynamic steady-state in (p).

increasing the normal load to N_2 (Fig. 10 (a) - (d)), and then the tangential load to T_2 (Figs. 10 (e) - (h)). A previous study presented the quasistatic strain fields present in an elastomeric roller due to normal loading using an undeformed reference image, as well as the strain fields due to tangential loading using a normally loaded reference image [48]. The strain field in Fig. 10 (d) agrees well with the normally loaded strain field in Ref. [48], while the strain field in Fig. 10 (h) is a combination of the normally and tangentially loaded strain fields in Ref. [48]. For quasistatic loading all data points in the region of interest (ROI) of the reference image remain within the deformed images, enabling direct application of Ncorr without the need for the dynamic two stage process presented in this work. However, once rolling is initiated, Ncorr is no longer sufficient due to material convection through the ROI, and thus the proposed dynamic method is required.

Figure 11 presents strain snapshots of the roller under $N_{0.5}$ and $T_{0.5}$ loads as it begins to rotate due to releasing the substrate constraint and subsequent stepper motor activation. We compile short videos which display the transition from quasistatic to dynamic steady-state. These videos are included in the Suplementary Information. See Vids. S4 - S6 for the $\varepsilon_{xx}, \varepsilon_{xy}$, and ε_{yy} for the $N_{0.5} + T_{0.5}$ loading scenario and Vids. S7 - S9 for the $N_2 + T_2$ loading scenario. The strain fields evolve from the quasistatic strain fields and then progress to a steady-state after a sufficient rolling distance. Figures 11 (a) - (h) document the evolution of the ε_{xx} strain field, Figs. 11 (i) - (l) the ε_{xy} strain field, and Figs. 11 (m) - (p) the ε_{yy} strain field. Each frame is labeled with the current angle of rotation of the roller. We extend the ε_{xx} strain fields out to 90° rotation to demonstrate that the roller has reached dynamic steady-state by frame (d). As documented in the figures, the strain fields undergo extensive qualitative changes during the start of rolling. In the quasistatic loading fields, the strain fields exhibit appreciable magnitude throughout the roller thickness, spanning from the roller hub to the rigid substrate. However, as the roller rotation begins, the strain magnitude (in particular, ε_{xx} and ε_{yy}) near the rigid hub decreases and appears to leave the field of view from left to right. At steady-state, the strain localizes to the contact region. Additionally, the steady-state rolling ε_{xx} strain field transitions to positive, tensile in the trailing edge of the contact region and negative, compressive in the leading edge.

The $N_2 + T_2$ loading scenario exhibits similar behavior. Figure 12 documents the strain field evolution during initiation of rolling. Figures 12 (a) - (h), (i) - (l), and (m) - (p) display the ε_{xx}, ε_{xy}, and ε_{yy} strains, respectively. We again extend the ε_{xx} strain fields out to 90° to show that a dynamic steady-state is reached by frame (d). The strain fields presented in Figs. 12 (a) - (p) settle into similar strain fields as those presented in Figs. 11 (a) - (p). The strain fields from the lighter loading scenario in Figs. 11 (a) - (p) experience maximum absolute strain points initially at the roller-hub interface during static loading before transitioning to the roller-substrate interface during rolling. The strain fields due to greater loading in Figs. 12 (a) - (p) initially experience maximum absolute strain at the roller-substrate interface which is preserved and amplified during rolling. While the locations of maximum absolute strain initially differ, under both loading scenarios the normal and shear strains settle into a dynamic steady-state where the regions of highest absolute strain are localized to the roller-substrate interface.

Focusing on the ε_{xx} strain fields in both the $N_{0.5} + T_{0.5}$ (Fig. 11 (a) - (h)) and $N_2 + T_2$ (Fig. 12 (a) - (h)) scenarios, we can interpret the behavior of the roller material as it transitions through the contact region. Initially, the applied counterclockwise induced torque results in a region of tension on the trailing edge of the stick zone while material builds up resulting in compression on the leading edge of stick zone. While the roller remains stationary, the material in the stick zone experiences no strain due to the presence of friction in the contact region preserving the original strain state of the roller material. However, as the roller begins to rotate, the material in tension due to the torque enters the stick zone where this tension state is preserved due to friction. This results in large tension regions developing at the interface of the roller and substrate, which is apparent in the strain fields. Once the material under tension has rotated

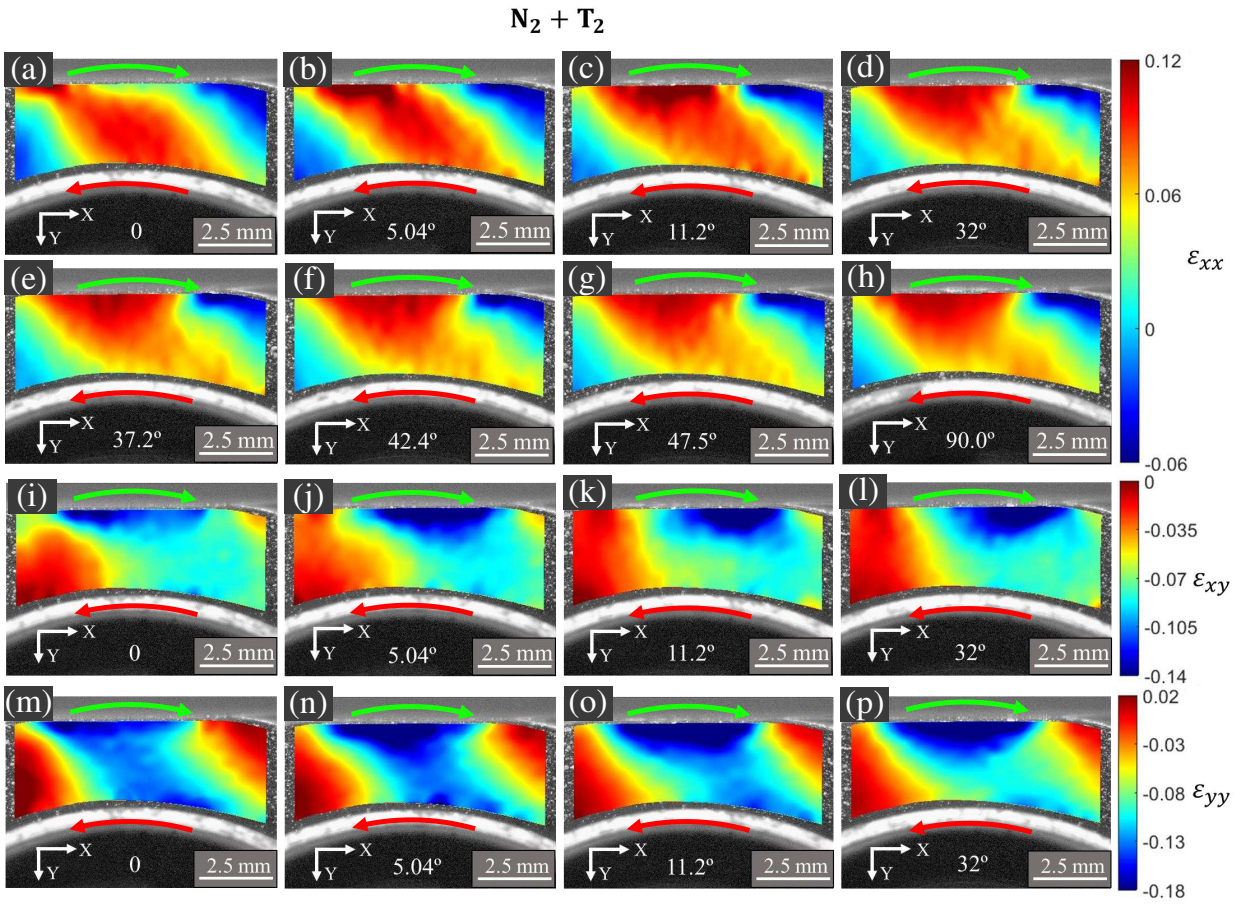

Figure 12: Strain fields produced during the onset of rolling when the roller transitions from quasistatic to dynamic steady-state for the $N_2 + T_2$ loading scenario. The rotation direction of the roller is marked as a green arrow above the roller in each image and the imposed torque due to the tangential load is marked as a red arrow on the roller hub. (a) - (h) ε_{xx} strain fields moving from quasistatic in (a) to dynamic steady-state in (d) - (h). (i) - (l) ε_{xy} strain fields moving from quasistatic in (i) to dynamic steady-state in (l). (m) - (p) ε_{yy} strain fields moving from quasistatic in (m) to dynamic steady-state in (p).

through the stick zone, it enters the slip zone where the material is free to release back to its natural form resulting in a small region of zero strain to the right of the large tension region. This relaxation is brief since it is rapidly pressed against its neighboring material due to the counter-clockwise torque combined with the substrate translating to the right in order to induce rotation.

We briefly explore how the strain fields in the roller change once the roller has stopped rotating due to halting the stepper motor rotation, effectively returning the roller to the quasistatic loading state. We include videos of the strain fields during motion arrest in the Supplementary Information. See Vids. S10 - S12 for the $\varepsilon_{xx}, \varepsilon_{xy}$, and ε_{yy} for the $N_{0.5} + T_{0.5}$ loading scenario and Vids. S13 - S15 for the $N_2 + T_2$ loading scenario. Notably, the dynamic steady-state strain fields are preserved once the roller motion ceases, illustrating the inherently nonlinear nature of the rolling contact problem whereby multiple, stable solutions arise from the same loading state.

7. Concluding Remarks

We have proposed a new DIC procedure capable of analyzing strain fields in scenarios where material convects through a region of interest. High resolution is achieved while avoiding the need to image the full body in both the reference and deformed images. We believe this procedure will be advantageous in dynamic contact problems such as the rolling contact problem demonstrated herein. Future work may utilize this procedure to analyze rolling contact during acceleration, braking, slipping, and time varying normal loads. While we have demonstrated the procedure using a rolling contact problem, the approach should be applicable to any scenario in which a deformable body undergoes large rotations and/or translations under applied loads.

Acknowledgements

This material is based upon work supported by the National Science Foundation under Grant No. 1916840.

References

[1] G Gao, W Yao, K Xia, and Z Li. Investigation of the rate dependence of fracture propagation in rocks using digital image correlation (dic) method. *Engineering Fracture Mechanics*, 138:146–155, 2015.

[2] Dongyang Li, Peiyan Huang, Zhanbiao Chen, Guowen Yao, Xinyan Guo, Xiaohong Zheng, and Yi Yang. Experimental study on fracture and fatigue crack propagation processes in concrete based on dic technology. *Engineering Fracture Mechanics*, 235:107166, 2020.

[3] Grzegorz Ludwik Golewski. Measurement of fracture mechanics parameters of concrete containing fly ash thanks to use of digital image correlation (dic) method. *Measurement*, 135:96–105, 2019.

[4] Cheng Zhao, Jinquan Xing, Yimeng Zhou, Zhenming Shi, and Gang Wang. Experimental investigation on hydraulic fracturing of granite specimens with double flaws based on dic. *Engineering Geology*, 267:105510, 2020.

[5] Huiheng Lian, Xinjian Sun, Zhenpeng Yu, Yaojie Lian, Lei Xie, Anxiong Long, and Zhixuan Guan. Study on the dynamic fracture properties and size effect of concrete based on dic technology. *Engineering Fracture Mechanics*, 274:108789, 2022.

[6] Shuting Miao, Peng-Zhi Pan, Shankun Zhao, Jun Han, and Petr Konicek. A new dic-based method to identify the crack mechanism and applications in fracture analysis of red sandstone containing a single flaw. *Rock Mechanics and Rock Engineering*, 54:3847–3871, 2021.

[7] Jiangtao Yu, Yichao Wang, Zhanhong Li, Qian Zhang, Xiangru Jian, and Zhigang Zhang. Using dic technique to characterize the mode ii interface fracture of layered system composed of multiple materials. *Composite Structures*, 230:111413, 2019.

[8] S Mallon, B Koohbor, A Kidane, and MA Sutton. Fracture behavior of prestressed composites subjected to shock loading: a dic-based study. *Experimental Mechanics*, 55:211–225, 2015.

[9] Kiran Kumar Namala, Puneet Mahajan, and Naresh Bhatnagar. Digital image correlation of low-velocity impact on a glass/epoxy composite. *International Journal for Computational Methods in Engineering Science and Mechanics*, 15(3):203–217, 2014.

[10] Ma Quanjin, MRM Rejab, Qayyum Halim, MNM Merzuki, and MAH Darus. Experimental investigation of the tensile test using digital image correlation (dic) method. *Materials Today: Proceedings*, 27:757–763, 2020.

[11] Lianxiang Yang PI, Lorenzo Smith, Mr Abhishek Gothekar, and Mr Xu Chen. Measure strain distribution using digital image correlation (dic) for tensile tests. *Oakland University*, 2010.

[12] Guillermo Valeri, Behrad Koohbor, Addis Kidane, and Michael A Sutton. Determining the tensile response of materials at high temperature using dic and the virtual fields method. *Optics and Lasers in Engineering*, 91:53–61, 2017.

[13] Wentao He, Changzi Wang, Shuqing Wang, Lu Yao, Linfeng Wang, and De Xie. Characterizing and predicting the tensile mechanical behavior and failure mechanisms of notched fmls—combined with dic and numerical techniques. *Composite Structures*, 254:112893, 2020.

[14] Zhubin He, Kun Zhang, Yanli Lin, and Shijian Yuan. An accurate determination method for constitutive model of anisotropic tubular materials with dic-based controlled biaxial tensile test. *International Journal of Mechanical Sciences*, 181:105715, 2020.

[15] Duane M Revilock Jr, John C Thesken, and Timothy E Schmidt. Three-dimensional digital image correlation of a composite overwrapped pressure vessel during hydrostatic pressure tests. In *2007 Semi Annual Conference and Exposition*, number E-16172, 2007.

[16] Leonardo D Rodrigues, JL Freire, Ronaldo D Vieira, and Jaime TP Castro. Strain analysis of thin pipe pressure vessels using digital image correlation. *J. Mech. Eng. Autom*, 4(2):63–72, 2014.

[17] Sachin Gupta, Venkitanarayanan Parameswaran, Michael A Sutton, and Arun Shukla. Study of dynamic underwater implosion mechanics using digital image correlation. *Proceedings of the Royal Society A: Mathematical, Physical and Engineering Sciences*, 470(2172):20140576, 2014.

[18] Michael Pinto, Sachin Gupta, and Arun Shukla. Study of implosion of carbon/epoxy composite hollow cylinders using 3-d digital image correlation. *Composite Structures*, 119:272–286, 2015.

[19] Wan Xu, Xiu Feng, Junrui Li, Xinfeng Shi, and Tian Bai. Strain analysis of pressure vessels contained pits based on digital image correlation method. In *Seventh International Symposium on Precision Mechanical Measurements*, volume 9903, pages 265–271. SPIE, 2016.

[20] Paweł Gąsior, Marcin Malesa, Jerzy Kaleta, Małgorzata Kujawińska, Krzysztof Malowany, and Radosław Rybczyński. Application of complementary optical methods for strain investigation in composite high pressure vessel. *Composite Structures*, 203:718–724, 2018.

[21] Sivakumar Palanivelu, Stefan De Pauw, Wim Van Paepegem, Joris Degrieck, Johan Van Ackeren, Dimitrios Kakogiannis, Jan Wastiels, Danny Van Hemelrijck, and John Vantomme. Validation of digital image correlation technique for impact loading applications. *Proc. DYMAT*, pages 373–379, 2009.

[22] RP Bigger, A Carpenter, N Scott, K Dannemann, S Chocron, and C Williams. Dynamic response of aluminum 5083 during taylor impact using digital image correlation. *Experimental Mechanics*, 58:951–961, 2018.

[23] Mark Flores, David Mollenhauer, Vipul Runatunga, Timothy Beberniss, Daniel Rapking, and Mark Pankow. High-speed 3d digital image correlation of low-velocity impacts on composite plates. *Composites Part B: Engineering*, 131:153–164, 2017.

[24] Peng Zhang and Maurizio Porfiri. A combined digital image correlation/particle image velocimetry study of water-backed impact. *Composite Structures*, 224:111010, 2019.

[25] Robin Chabrier, E Sadoulet-Reboul, Gael Chevallier, Emmanuel Foltête, and Thomas Jeannin. Full-field measurements with digital image correlation for vibro-impact characterisation. *Mechanical Systems and Signal Processing*, 156:107658, 2021.

[26] Jan De Pauw, Wim De Waele, Reza Hojjati-Talemi, and Patrick De Baets. On the use of digital image correlation for slip measurement during coupon scale fretting fatigue experiments. *International Journal of Solids and Structures*, 51(18):3058–3066, 2014.

[27] Yue Su, Shao-Shi Rui, Qi-Nan Han, Zhi-Hao Shang, Li-Sha Niu, Hao Li, Hiroshi Ishikawa, and Hui-Ji Shi. Estimation method of relative slip in fretting fatigue contact by digital image correlation. *Metals*, 12(7):1124, 2022.

[28] J Juoksukangas, A Lehtovaara, and A Mäntylä. Applying the digital image correlation method to fretting contact for slip measurement. *Proceedings of the Institution of Mechanical Engineers, Part J: Journal of Engineering Tribology*, 231(4):509–519, 2017.

[29] Mehmet E Kartal, Daniel M Mulvihill, David Nowell, and David A Hills. Determination of the frictional properties of titanium and nickel alloys using the digital image correlation method. *Experimental Mechanics*, 51:359–371, 2011.

[30] DM Mulvihill, H Brunskill, ME Kartal, RS Dwyer-Joyce, and D Nowell. A comparison of contact stiffness measurements obtained by the digital image correlation and ultrasound techniques. *Experimental Mechanics*, 53:1245–1263, 2013.

[31] Ari J Tuononen. Digital image correlation to analyse stick–slip behaviour of tyre tread block. *Tribology International*, 69:70–76, 2014.

[32] Xue-Liang Gao, Ye Zhuang, Shu Liu, Chen-Wei Zhu, and Qiang Chen. Digital image correlation to analyze slip state of tire tread block in the cornering condition. *Optik*, 185:571–584, 2019.

[33] Milosz K Rajchel, Michael Varenberg, Michael J Leamy, and Antonia Antoniou. Instrument for in situ study of rolling under normal load and torque. *Review of Scientific Instruments*, 93(9):093705, 2022.

[34] Theunis R Botha and P Schalk Els. Digital image correlation techniques for measuring tyre-road interface parameters: Part 1–side-slip angle measurement on rough terrain. *Journal of Terramechanics*, 61:87–100, 2015.

[35] T Botha, B Shyrokau, PS Els, and E Holweg. Kinematic analysis of a tyre rolling over rough terrain using digital image correlation. In *Proc. of 13th European Conference of the International Society of Terrain-Vehicle System, Rome, Italy*, 2015.

[36] S Galeazzi, P Chiariotti, M Martarelli, and EP Tomasini. 3d digital image correlation for vibration measurement on rolling tire: procedure development and comparison with laser doppler vibrometer. In *Journal of Physics: Conference Series*, volume 1149, page 012010. IOP Publishing, 2018.

[37] Xueliang Gao, Ye Zhuang, Shu Liu, Weiguang Fan, Chengwei Zhu, and Qiang Chen. High-speed 3d digital image correlation for rolling deformation of a tire sidewall and measuring dynamic contact patch length. *Applied Optics*, 59(5):1313–1322, 2020.

[38] Xueliang Gao, Ye Zhuang, and Shu Liu. High-speed 3d digital image correlation for measuring tire rolling resistance coefficient. *Measurement*, 171:108830, 2021.

[39] Xueliang Gao, Yi Xiong, Weiping Liu, and Ye Zhuang. Modeling and experimental study of tire deformation characteristics under high-speed rolling condition. *Polymer Testing*, 99:107052, 2021.

[40] Ahmed A Shabana. Computer implementation of the absolute nodal coordinate formulation for flexible multibody dynamics. *Nonlinear Dynamics*, 16:293–306, 1998.

[41] Mohammadreza Vaziri Sereshk and Mahmoud Salimi. Comparison of finite element method based on nodal displacement and absolute nodal coordinate formulation (ancf) in thin shell analysis. *International journal for numerical methods in biomedical engineering*, 27(8):1185–1198, 2011.

[42] Lianpo Wang, Songlin Bi, Hui Li, Yonggang Gu, and Chao Zhai. Fast initial value estimation in digital image correlation for large rotation measurement. *Optics and Lasers in Engineering*, 127:105838, 2020.

[43] F Zhong and C Quan. Digital image correlation in polar coordinate robust to a large rotation. *Optics and Lasers in Engineering*, 98:153–158, 2017.

[44] Stefan Leutenegger, Margarita Chli, and Roland Y Siegwart. Brisk: Binary robust invariant scalable keypoints. In *2011 International conference on computer vision*, pages 2548–2555. Ieee, 2011.

[45] J Blaber, B Adair, and Antonia Antoniou. Ncorr: open-source 2d digital image correlation matlab software. *Experimental Mechanics*, 55(6):1105–1122, 2015.

[46] Michael Leamy Nehemiah Mork, Antonia Antoniou. Dynamic dic. *https://sourceforge.net/projects/dynamic-dic/files/*, (created: 2024-12-06).

[47] Azra Fetić, Davor Jurić, and Dinko Osmanković. The procedure of a camera calibration using camera calibration toolbox for matlab. In *2012 Proceedings of the 35th International Convention MIPRO*, pages 1752–1757. IEEE, 2012.

[48] Nehemiah Mork, Milosz K Rajchel, Michael Varenberg, Antonia Antoniou, and Michael J Leamy. Quasistatic strain fields in normaly- and tangentially-loaded elastomeric rollers under impending slip. *International Journal of Solids and Structures*, 292:112739, 2024.

[49] Shaharyar Ahmed Khan Tareen and Zahra Saleem. A comparative analysis of sift, surf, kaze, akaze, orb, and brisk. In *2018 International conference on computing, mathematics and engineering technologies (iCoMET)*, pages 1–10. IEEE, 2018.

[50] James Kennedy and Russell Eberhart. Particle swarm optimization. In *Proceedings of ICNN'95-international conference on neural networks*, volume 4, pages 1942–1948. IEEE, 1995.

[51] Federico Marini and Beata Walczak. Particle swarm optimization (pso). a tutorial. *Chemometrics and Intelligent Laboratory Systems*, 149:153–165, 2015.

[52] Tareq M Shami, Ayman A El-Saleh, Mohammed Alswaitti, Qasem Al-Tashi, Mhd Amen Summakieh, and Seyedali Mirjalili. Particle swarm optimization: A comprehensive survey. *IEEE Access*, 10:10031–10061, 2022.